Kibble-Zurek Dynamics in the Anisotropic Ising Model of the Si(001) Surface

G. Schaller,[1] F. Queisser,[1] S. P. Katoorani,[1] C. Brand,[2] C. Kohlfürst,[1] M. R. Freeman,[3] A. Hucht,[2] P. Kratzer,[2] B. Sothmann,[2] M. Horn-von Hoegen,[2] and R. Schützhold[1,4]

[1]*Helmholtz-Zentrum Dresden-Rossendorf, Bautzner Landstraße 400, 01328 Dresden, Germany*

[2]*Fakultät für Physik, Universität Duisburg-Essen and CENIDE, Lotharstraße 1, 47057 Duisburg, Germany*

[3]*Department of Physics, University of Alberta, 4-181 Centennial Center for Interdisciplinary Science Edmonton, Alberta T6G 2E1, Canada*

[4]*Institut für Theoretische Physik, Technische Universität Dresden, 01062 Dresden, Germany*

(Received 1 July 2024; revised 27 January 2025; accepted 15 May 2025; published 17 June 2025)

As a simplified description of the nonequilibrium dynamics of buckled dimers on the Si(001) surface, we consider the anisotropic two-dimensional (2D) Ising model and study the freezing of spatial correlations during a cooling quench across the critical point. Depending on the cooling rate, we observe a crossover from one-dimensional (1D) to 2D behavior. For rapid cooling, we find effectively 1D behavior in the strongly coupled direction, for which we provide an exact analytic solution of the nonequilibrium dynamics. For slower cooling rates, we start to see 2D behavior where our numerical simulations show an approach to the usual Kibble–Zurek scaling in 2D.

DOI: 10.1103/rmc4-xqb3

Introduction—Von Neumann once [1] compared nonequilibrium theory to a theory of nonelephants—indicating the richness and complexity of this field, which we are just beginning to understand. In view of the diverging response time near the critical point, continuous phase transitions are prototypical candidates for observing nonequilibrium behavior [2,3]. A prominent example is the Kibble mechanism describing the formation of topological defects during symmetry-breaking phase transitions in the early universe [4]. Later Zurek realized that quite analogous effects should also occur in condensed matter such as superfluid helium [5]. The Kibble–Zurek mechanism has been studied in numerous theoretical (e.g., [6–24]) and experimental investigations (e.g., [25–35]). An important point is the transition from adiabatic evolution to nonequilibrium behavior (such as freezing) when approaching or traversing the critical point. Apart from the original idea of creating topological defects, the general mechanism can also be applied to the frozen domain structure in symmetry-breaking phase transitions induced by the critical slowing down.

In this Letter, we study the anisotropic Ising model in two spatial dimensions [36–43] with special emphasis on possible differences between the two directions. Apart from advancing our fundamental understanding, these investigations are also motivated by the fact that the buckling dynamics of dimers on the Si(001) surface can be described by the anisotropic two-dimensional (2D) Ising model [44–53]. Here, we consider the transition from the $p(2\times 1)$ to the $c(4\times 2)$ reconstruction at a critical temperature $T_{\mathrm{crit}} \approx 190$ K. Since the (001) face of single-crystalline silicon belongs to the most important surfaces both in technology and science, our results will also be relevant in this regard. For example, the dependence of the frozen

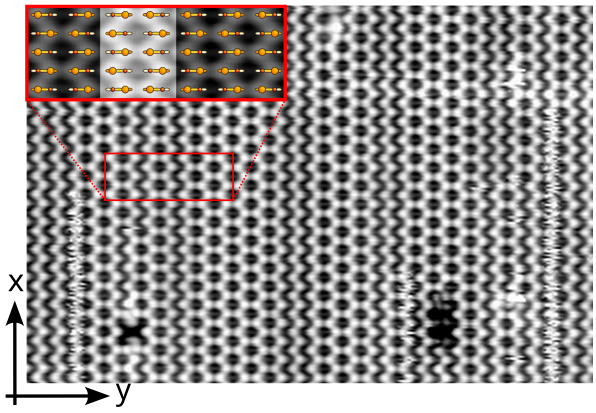

FIG. 1. Low-temperature scanning tunneling microscope (STM) image of a Si(001) surface taken at 5 K with $U_{\mathrm{bias}} = 1.3$ V and $I_{\mathrm{tunnel}} = 1$ nA. Field of view is 24×16 nm^2. Areas with $c(4\times 2)$ reconstruction exhibit a "honeycomb" pattern, whereas domain boundaries can be identified by a zigzag chain of local $p(2\times 2)$ reconstruction, with dimer buckling and resulting domains (vertically running rows) indicated in the inset. The two dark spots are frozen horizontal domain boundaries, while frizzy vertical lines correspond to active phase boundary changes, i.e., mobile "phasons" [56].

domain structure on the cooling rate indicates how sufficiently homogeneous Si(001) surfaces should be prepared.

Experimental observations—Let us start by presenting experimental evidence for the formation of frozen domain structures on the Si(001) dimerized surface. The surface exhibits parallel rows of alternately buckled dimers, which arrange in a $c(4\times 2)$ reconstruction indicating the anti-phase correlation between neighboring dimer rows [54,55]. Figure 1 shows a low-temperature scanning tunneling microscopy (STM) image taken at 5 K after preparation of the Si(001) surface through flash annealing and rapid cooldown across $T_{\rm crit}$ to liquid nitrogen temperatures $T < 100$ K. Further experimental details can be found elsewhere [56]. The STM image was taken at constant current conditions with positive sample bias, i.e., in Fig. 1 filled orbitals of the Si atoms are displayed in bright gray. Along each vertically running row, the alternating buckling can be nicely identified. The anti-phase correlation between neighboring dimers cause the $c(4\times 2)$ reconstruction, which becomes apparent as a "honeycomb" pattern.

During the rapid cooldown subsequent to sample preparation, the regime of critical slowing down [57,58] is reached near $T_{\rm crit}$, where the system falls out of equilibrium, resulting in a frozen domain structure, which is apparent in Fig. 1. The domain boundaries can be identified as one-dimensional (1D) "defects" separating ordered areas with a $c(4\times 2)$ reconstruction. As also confirmed by electron diffraction [52,53], these ordered domains are extremely elongated, i.e., the frozen correlation length $\xi_\parallel$ along the dimer rows, i.e., in vertical direction, is much larger than the horizontal one $\xi_\perp$ across the rows.

For a rough estimate of the correlation lengths $\xi_\parallel$ and $\xi_\perp$, we may count the average number of lattice sites between two defects in Fig. 1. Horizontally, this yields a correlation length $\xi_\perp$ between two and three lattice sites, whereas $\xi_\parallel$ is much longer, larger than 50 lattice sites. Thus, the anisotropy ratio $\xi_\parallel/\xi_\perp$ observed in Fig. 1 is significantly larger than the ratio of 10:1 as expected from the standard Kibble–Zurek mechanism (as explained below and in Supplemental Material [59]).

Anisotropic Ising model—In order to understand the behavior of the correlation lengths mentioned above, we need to model the nonequilibrium dynamics of buckled dimers on the Si(001) surface, which form a rectangular lattice. If we describe the tilt of the dimer at lattice site $i,j\in\mathbb{Z}$ to the left or the right by the pseudo-spin variable $\sigma_{i,j}=+1$ or $\sigma_{i,j}=-1$, respectively, the resulting energy for the pseudo-spin configuration $\boldsymbol{\sigma}$ corresponds to the anisotropic Ising model [44–46,48–51]

$$E_{\boldsymbol{\sigma}} = -J_x\sum_{i,j}\sigma_{i,j}\sigma_{i+1,j} - J_y\sum_{i,j}\sigma_{i,j}\sigma_{i,j+1} - J_{\rm d}\sum_{i,j}\sigma_{i,j}[\sigma_{i+1,j+1}+\sigma_{i+1,j-1}]. \quad (1)$$

Combining microscopic considerations with experimental data, a strong antiferromagnetic coupling along dimer rows $J_x\approx -25$ meV and weaker couplings across rows $J_y\approx 3.2$ meV and in diagonal direction $J_{\rm d}\approx 2.0$ meV have been found [52,53]. The latter two can be combined into an effective transversal coupling $J_\perp = J_y - 2J_{\rm d}\approx -0.8$ meV. As a result, the actual surface favors antiferromagnetic order in both directions. For convenience, however, we apply a checkerboard transformation $\sigma_{i,j}\to(-1)^{i+j}\sigma_{i,j}$ after which both $J_\parallel = J_x$ and $J_\perp$ are positive and the transformed model favors ferromagnetic order.

Rate equations—We study the nonequilibrium dynamics of the Ising model (1) via standard rate equations for the probabilities $P_{\boldsymbol{\sigma}}$ of the pseudo-spin configurations $\boldsymbol{\sigma}$

$$\dot{P}_{\boldsymbol{\sigma}} = \sum_{\boldsymbol{\sigma}'}[R_{\boldsymbol{\sigma}'\to\boldsymbol{\sigma}}P_{\boldsymbol{\sigma}'} - R_{\boldsymbol{\sigma}\to\boldsymbol{\sigma}'}P_{\boldsymbol{\sigma}}]. \quad (2)$$

Neglecting correlated flips of two or more pseudo-spins (i.e., dimers), we use single-flip transition rates

$$R_{\boldsymbol{\sigma}'\to\boldsymbol{\sigma}} = \frac{\Gamma\exp\{-\beta E_{\rm B}\}}{\exp\{\beta(E_{\boldsymbol{\sigma}}-E_{\boldsymbol{\sigma}'})\}+1}. \quad (3)$$

The "knocking" frequency $\Gamma\approx 10^{12}/\mathrm{s}$ and Arrhenius barrier height $E_{\rm B}\approx 100$ meV are obtained from microscopic considerations [53,56,60]. The Glauber factor in the denominator [61,62] can also be motivated by microscopic models for surface-bulk interactions, e.g., in the form of a reservoir of two-level systems [63] or via fermionic tunneling [64]. It ensures that the rate is bounded $R_{\boldsymbol{\sigma}'\to\boldsymbol{\sigma}} < \Gamma\exp\{-\beta E_{\rm B}\}$ and satisfies the detailed balance condition $R_{\boldsymbol{\sigma}'\to\boldsymbol{\sigma}}/R_{\boldsymbol{\sigma}\to\boldsymbol{\sigma}'} = \exp\{-\beta(E_{\boldsymbol{\sigma}}-E_{\boldsymbol{\sigma}'})\}$, which enforces evolution toward thermal equilibrium for constant parameters Γ and β etc.

1D Ising model—Now we are in the position to study the nonequilibrium dynamics of the Ising model (1) during a cooling quench $\beta\to\beta(t)$. As the first step, we consider a very rapid cooling rate such that the system basically has no time for an exchange between the dimer rows, i.e., in the weakly coupled direction. Then, as also confirmed by numerical simulations (see Fig. 2), we may consider the limiting case $J_y\to 0$ and $J_{\rm d}\to 0$ of the 2D Ising model (1) such that each row j separately forms a 1D Ising model with $J = J_x = J_\parallel$

$$E^{\rm 1D}_{\boldsymbol{\sigma}} = -J\sum_i \sigma_i\sigma_{i+1}, \quad (4)$$

where after the checkerboard transformation $J>0$. Assuming translational invariance, we may derive an exact evolution equation for the correlator $c_a = \langle\sigma_i\sigma_{i+a}\rangle$ depending on distance a. With the dimensionless conformal time coordinate $d\mathfrak{T}/dt = \Gamma e^{-\beta(t)E_{\rm B}}$ we find (with the boundary condition $c_{a=0}=1$) [59]

$$\partial_{\mathfrak{T}}c_a = -2c_a + (c_{a+1}+c_{a-1})\tanh[2\beta(\mathfrak{T})J]. \quad (5)$$

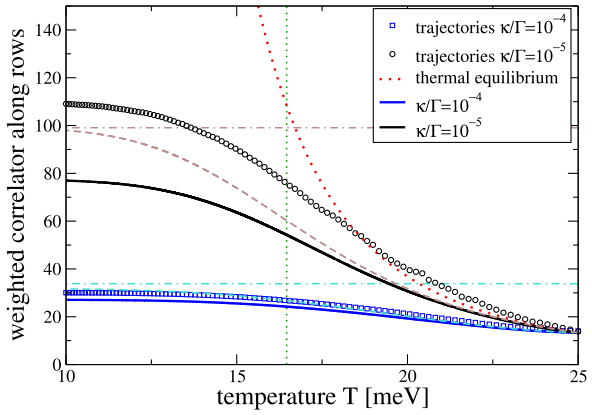

FIG. 2. Freezing of the weighted sum of correlations $\mathfrak{C}$ for cooling quenches $T(t) = T_{\text{in}} e^{-\kappa t}$. The black solid curve represents the numeric solution of Eq. (6) for the 1D Ising model (4) for $\kappa = 10^7\,\text{s}^{-1}$ and the solid blue curve for $\kappa = 10^8\,\text{s}^{-1}$, while the symbols correspond to full numerical simulations of the 2D Ising model (1) on a 1600×200 lattice averaged over 100 trajectories. Correlations between rows remain weak for these parameters (see below). The dotted red curve depicts the thermal equilibrium value in 1D and the dashed curves and dash-dotted horizontal lines in lighter colors represent the analytic solutions of the equation $\partial_{\mathfrak{T}}\mathfrak{C} = \lambda\mathfrak{T}\mathfrak{C} + 1$ and the approximations $\mathfrak{C}_{\text{freeze}} \approx \sqrt{\pi/(2\lambda)}$ to the frozen values discussed in the text [59]. The vertical dotted line depicts the critical temperature in 2D.

Setting the left-hand side to zero yields the well-known equilibrium solution $c_a = [\tanh(\beta J)]^{|a|}$. The 1D Ising model (4) does not have a critical point at finite temperature $T_{\text{crit}} > 0$; instead the analog of a critical point occurs at zero temperature $T_{\text{crit}} = 0$ where the correlation length ξ diverges as $\xi \sim e^{2\beta J}$ [38].

In order to understand the nonequilibrium dynamics governed by Eq. (5), let us consider the continuum limit, where $c_{a+1} + c_{a-1} - 2c_a$ becomes the second spatial derivative such that we obtain a diffusion-dissipation equation $\partial_{\mathfrak{T}} c = \mathfrak{D}\partial_x^2 c - \gamma c$. For large temperatures, the diffusion coefficient is small $\mathfrak{D} \propto \tanh(2\beta J) \approx 2\beta J \ll 1$ and the damping term $\gamma \approx 2$ dominates. For small temperatures, the damping rate $\gamma = 2 - 2\tanh(2\beta J)$ is suppressed as $4e^{-4\beta J}$ and the diffusion term $\mathfrak{D} \propto \tanh(2\beta J) \approx 1$ dominates. Thus, we may introduce a response or relaxation time $\mathfrak{T}_{\text{relax}}$ from the inverse damping rate $1/\gamma$, which then scales as $\mathfrak{T}_{\text{relax}} \sim e^{4\beta J}$, i.e., $\mathfrak{T}_{\text{relax}} \sim \xi^2$. Note, however, that the diffusion coefficient stays finite even for $\mathfrak{T}_{\text{relax}} \to \infty$, i.e., diffusion is still possible.

Freezing in 1D—Since analyzing the nonequilibrium dynamics by means of analytic solutions of Eq. (5) is still quite involved, let us consider the weighted sum of correlations $\mathfrak{C} = \sum_{a=1}^{\infty} a c_a$, which obeys

$$\partial_{\mathfrak{T}}\mathfrak{C} = -2[1 - \tanh(2\beta J)]\mathfrak{C} + \tanh(2\beta J). \tag{6}$$

In order to provide an explicit example and to study the analog of critical slowing down, let us assume the simple cooling protocol $T(t) = T_{\text{in}} e^{-\kappa t}$ or $\beta(t) = \beta_{\text{in}} e^{\kappa t}$ starting at an initial temperature T_{in} and cooling down to zero temperature at $t \to \infty$. This protocol can be motivated by assuming that the system is cooled down via ordinary thermal conduction to a cold reservoir, for example. Then the conformal time is given by the exponential integral $\mathfrak{T}(t) = \text{Ei}(-e^{\kappa t} E_{\text{B}}/T_{\text{in}})\Gamma/\kappa$ and the infinite interval of laboratory time $t \in (0, \infty)$ is mapped to a finite interval of conformal time $\mathfrak{T} \in (\mathfrak{T}_{\text{in}}, 0)$.

Incidentally, for our values with $E_{\text{B}} \approx 4J_x$ and assuming $E_{\text{B}} \gg T_{\text{in}}$, we may simplify Eq. (6) even further. In this limit, we may approximate the exponential integral by its asymptotic behavior $\text{Ei}(-z) \approx -e^{-z}/z$ and Eq. (6) becomes $\partial_{\mathfrak{T}}\mathfrak{C} \approx \lambda\mathfrak{T}\mathfrak{C} + 1$ with $\lambda = 4\kappa E_{\text{B}}/(T_{\text{in}}\Gamma)$. The solution to this equation can be given in terms of the error function [59], but we may understand its behavior by means of general arguments. Since we have $|\mathfrak{T}_{\text{in}}| \gg 1$ for our parameters, let us start at $\mathfrak{T}_{\text{in}} \to -\infty$. First, $\mathfrak{C}$ approaches its instantaneous equilibrium value $\mathfrak{C}_{\text{eq}} = 1/|\lambda\mathfrak{T}|$. However, once the response time $\mathfrak{T}_{\text{relax}} \sim 1/|\lambda\mathfrak{T}|$ becomes too short $\mathfrak{T}_{\text{relax}} \sim |\mathfrak{T}|$, the system cannot equilibrate anymore and thus the value of $\mathfrak{C}$ freezes in at $\mathfrak{T}_{\text{freeze}} \sim 1/\sqrt{\lambda}$ to its final value $\mathfrak{C}_{\text{freeze}} \approx \sqrt{\pi/(2\lambda)}$. Furthermore, as $\mathfrak{C}$ scales with the square of the correlation length ξ, we obtain $\xi_{\text{freeze}} \sim \lambda^{-1/4} \sim \kappa^{-1/4}$, which is the analog to the Kibble–Zurek scaling for this case. For example, for the value of $\kappa = 10^7\,\text{s}^{-1}$ used in the solid black curve in Fig. 2, we have $\lambda = \mathcal{O}(10^{-4})$ and thus $\xi_{\text{freeze}} = \mathcal{O}(10)$. Comparison with Fig. 1 indicates that the cooling rate in the experiment must have been smaller.

2D Ising model—As the next step, let us study slower cooling rates, where we start to see two-dimensional behavior. For simplicity, we consider the two-dimensional Ising model in terms of the effective transversal coupling strength $J_\perp$ introduced above

$$E_{\boldsymbol{\sigma}}^{\text{2D}} = -J_{\parallel}\sum_{i,j}\sigma_{i,j}\sigma_{i+1,j} - J_\perp\sum_{i,j}\sigma_{i,j}\sigma_{i,j+1}. \tag{7}$$

The equilibrium properties of this model can be obtained by Onsager theory [65]. Its critical temperature $T_{\text{crit}} = 1/(k_{\text{B}}\beta_{\text{crit}})$ is determined by the relation $\sinh(2\beta_{\text{crit}}|J_{\parallel}|)\sinh(2\beta_{\text{crit}}|J_\perp|) = 1$. Thus, in the limit of strong anisotropy $J_{\parallel} \gg J_\perp$, we obtain the hierarchy of scales $J_{\parallel} \gg \beta_{\text{crit}}^{-1} \gg J_\perp$. Approaching the critical point from above, the correlation lengths $\xi_{\parallel}$ and $\xi_\perp$ in x and y direction (i.e., along the dimer rows and perpendicular to them) both obey the scaling $|T - T_{\text{crit}}|^{-\nu}$ with the critical exponent $\nu = 1$, though with different prefactors [37,40]. In particular, their ratio stays constant and is given by $\xi_\perp^{\text{eq}}/\xi_{\parallel}^{\text{eq}} = \sinh(2\beta_{\text{crit}}J_\perp) \approx 2\beta_{\text{crit}}J_\perp \approx 0.1$. Thus, in the standard Kibble–Zurek picture [59] where both correlations freeze at time $\mathfrak{T}_{\text{freeze}}$, one would expect the same ratio for their frozen values.

Now considering the correlator $c_{a,b} = \langle \sigma_{i,j}\sigma_{i+a,j+b}\rangle$ and its evolution equation analogous to Eq. (5), we find that the terms on the right-hand side containing $J_\perp$ do also involve four-point correlators such as $\langle \sigma_{i,j}\sigma_{k-1,\ell}\sigma_{k+1,\ell}\sigma_{k,\ell\pm1}\rangle$. To close this set of equations approximately, we may apply a perturbative expansion scheme and neglect terms of order $J_\perp^2$ [59]. Then, since the four-point correlators have already a small prefactor $\sim J_\perp$ out front, we may approximate them by their zeroth order $\langle \sigma_{i,j}\sigma_{k-1,\ell}\sigma_{k+1,\ell}\sigma_{k,\ell\pm1}\rangle \approx \langle \sigma_{i,j}\sigma_{k,\ell\pm1}\rangle\langle \sigma_{k-1,\ell}\sigma_{k+1,\ell}\rangle$ where the short-range correlations $\langle \sigma_{k-1,\ell}\sigma_{k+1,\ell}\rangle$ within a row ℓ can be approximated by their equilibrium value $\langle \sigma_{k-1,\ell}\sigma_{k+1,\ell}\rangle \approx \tanh^2(\beta J_\parallel)$ in 1D (as discussed above). After that, we obtain an approximate diffusion-dissipation equation in 2D

$$\partial_{\mathfrak{T}} c_{a,b} = -2c_{a,b} + (c_{a+1,b} + c_{a-1,b})\tanh(2\beta J_\parallel) + \beta J_\perp^{\mathrm{eff}}(c_{a,b+1} + c_{a,b-1}) + \mathcal{O}(J_\perp^2), \tag{8}$$

but with a strongly reduced transversal coupling strength $J_\perp^{\mathrm{eff}} = 2J_\perp/\cosh(2\beta J_\parallel)$. As an intuitive picture, the preexistent strong in-row correlation requires many spin flips for cross-row equilibration and thus renders this process very hard. In the continuum limit, the ratio between the effective diffusion coupling strengths $\mathfrak{D}_\parallel \propto \tanh(2\beta J_\parallel)$ and $\mathfrak{D}_\perp \propto \beta J_\perp^{\mathrm{eff}}$ in the two directions in Eq. (8) determines the ratio of the equilibrium correlation lengths, which is consistent with the results above $\xi_\perp^{\mathrm{eq}}/\xi_\parallel^{\mathrm{eq}} = \sqrt{\mathfrak{D}_\perp/\mathfrak{D}_\parallel} = \sqrt{2\beta J_\perp/\sinh(2\beta J_\parallel)} \approx 2\beta_{\mathrm{crit}} J_\perp$ close to the critical point.

In the nonequilibrium case, Eq. (8) allows us to understand the crossover from 1D to 2D. Inserting our values, we find $\beta_{\mathrm{crit}} J_\perp^{\mathrm{eff}}|_{\mathrm{crit}} \approx 0.01$, which explains why a time interval of $|\mathfrak{T}_{\mathrm{in}}| \approx 37.8$ (solid blue curve in Fig. 2) is too short to generate correlations between the rows. Only for slower sweep rates, such as $|\mathfrak{T}_{\mathrm{in}}| \approx 378$ (solid black curve in Fig. 2), these correlations start to build up, even though they are still very weak. Actually, by employing time-dependent perturbation theory in $J_\perp$ via inserting the time-dependent (nonequilibrium) correlator $\langle \sigma_{k-1,\ell}\sigma_{k+1,\ell}\rangle \approx c_{a=2}(t)$ within a row ℓ obtained from the exact 1D solution discussed in Eq. (5) into the evolution equation for $\partial_{\mathfrak{T}} c_{a,b}$, we can describe the buildup of correlations between rows reasonably well for fast and intermediate sweep rates up to $\kappa = 10^6\,\mathrm{s}^{-1}$ [59].

Numerical simulations—Finally, let us compare the analytical approximation schemes discussed above to a full numerical simulation of Eqs. (1)–(3) with time-dependent $\beta(t)$ [59]. Because of the exponential dimensionality of (2) for an $N_x \times N_y$ spin lattice, we calculate trajectory solutions. For a given configuration $\boldsymbol{\sigma}$, we propagate time by the stochastic waiting time $\tau_{\boldsymbol{\sigma}}$ found by numerically solving $\ln(1-r) = -\sum_{\boldsymbol{\sigma}'} \int_t^{t+\tau_{\boldsymbol{\sigma}}} R_{\boldsymbol{\sigma}\to\boldsymbol{\sigma}'}(t')dt'$, with uniformly distributed random number $r \in [0,1]$, and perform a jump to a different state with the conditional probability [66,67] given by $P_{\boldsymbol{\sigma}\to\boldsymbol{\sigma}'} = R_{\boldsymbol{\sigma}\to\boldsymbol{\sigma}'}/[\sum_{\boldsymbol{\sigma}''\neq\boldsymbol{\sigma}} R_{\boldsymbol{\sigma}\to\boldsymbol{\sigma}''}]$ at time $t+\tau_{\boldsymbol{\sigma}}$. In the selection of jumps, we use [68] that the $N_x N_y$ different single-spin flip processes can be grouped into 45 classes with identical energy differences entering the rates (3). Eventually, denoting the fast Fourier transformed spin lattice by $\tilde{\sigma}_{k_x k_y}$, the correlation lengths $\xi_\parallel$ and $\xi_\perp$ are then given by the inverse widths of the one-dimensional lattices $\sum_{k_y} |\tilde{\sigma}_{k_x k_y}|^2$ and $\sum_{k_x} |\tilde{\sigma}_{k_x k_y}|^2$, respectively. Averaging over multiple trajectories (and the resulting $|\tilde{\sigma}_{k_x k_y}|^2$) can be used to improve the statistics.

In Fig. 3, we contrast the time-dependent averaged correlation lengths (connected symbols and solid curves) with equilibrium versions (symbols) for exponential and linear cooling protocols (starting after an equilibration phase). Already at temperatures above T_{crit}, the correlation lengths depart from their equilibrium limits, but furthermore we see that this happens earlier for the weakly coupled direction.

The final (i.e., frozen) correlation lengths are depicted in Fig. 4 as a function of the inverse cooling rate Γ/κ for exponential (circle symbols) and linear (square symbols)

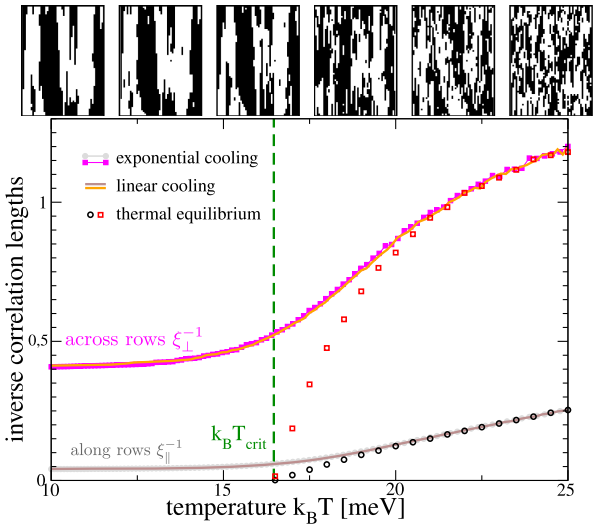

FIG. 3. Plot of inverse correlation lengths versus temperature (or, equivalently, time) for exponential $T(t) = T_{\mathrm{in}} e^{-\kappa t}$ (connected symbols) and linear $T(t) = T_{\mathrm{in}} - \eta t$ (solid curves) cooling sweeps. Choosing $\eta = \kappa T_{\mathrm{crit}}$ ensures that the cooling rates at the critical points coincide; as a result, the curves for the two protocols lie almost on top of each other. The value $\eta = \kappa T_{\mathrm{crit}} = 174 \times 10^6\,\mathrm{K/s}$ used here corresponds to $\Gamma/\kappa \approx 10^6$ in Fig. 4. The results are obtained for a $16,000 \times 2000$ lattice, averaged over 100 trajectories. The correlation length $\xi_\perp$ in weakly coupled direction departs earlier than the other $\xi_\parallel$ from the equilibrium solutions (red squares and black circles). On top, we added lattice portion snapshots of 67×50 pseudo-spins showing the (exponential protocol) time evolution of an example configuration at the respective temperatures as an illustration.

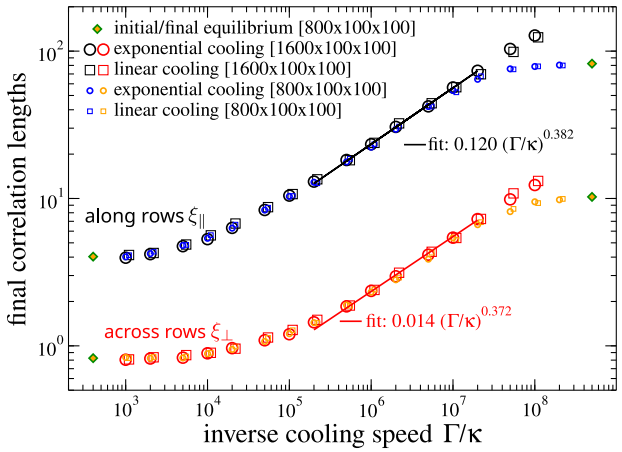

FIG. 4. Plot of the final (frozen) correlation lengths for different lattice sizes and averaged over 100 trajectories $[N_x \times N_y \times N_{\mathrm{trj}}]$ versus the inverse critical cooling speed Γ/κ for exponential [$T(t) = T_{\mathrm{in}} e^{-\kappa t}$, circle symbols] and linear [$\mathrm{T(t)} = \mathrm{T_{in}} - \eta t$ with $\eta = \kappa T_{\mathrm{crit}}$ as in Fig. 3, square symbols] protocols, all cooling the system down from $k_{\mathrm{B}} T_{\mathrm{in}} = 25$ meV to $k_{\mathrm{B}} T_{\mathrm{fi}} = 10$ meV. For too fast protocols (left), the system can never follow, but Kibble–Zurek scaling is recovered for intermediate protocol times. Finite-size effects are visible for slow protocols (small vs. large symbols).

cooling protocols. For extremely fast sweeps $\Gamma/\kappa < 10^3$, the system cannot follow and basically remains at the initial equilibrium values. However, already for $\Gamma/\kappa = \mathcal{O}(10^4)$, we start observing a growth of $\xi_{\parallel}$ while $\xi_{\perp}$ is still negligible, i.e., effectively 1D behavior (cf. the blue curve in Fig. 2). For intermediate-speed sweeps, such as $\Gamma/\kappa = \mathcal{O}(10^6)$, we find that both final correlation lengths follow a universal power-law increase, consistent with the Kibble–Zurek exponent $\nu/(1 + z\nu) \approx 1/3$ (see the fitted regions in Fig. 4). For very slow sweeps, we find that finite-size effects start to play a role. Experimentally, such finite-size effects may origin from the omnipresent steps of a real Si(001) surface [69], which ultimately limit the correlation lengths at low cooling rates. As we are interested in higher cooling rates in order to observe the frozen domain structure, this can be safely avoided for samples with low miscut; we have used a wafer with $< \pm 0.25°$ precision in Fig. 1.

Conclusions—As a model for the buckling dynamics of dimers on Si(001) surfaces, we consider the anisotropic Ising model in 2D and study the freezing of spatial correlations (which determine the final domain structure) when cooling through the critical point via $\beta(t) = \beta_{\mathrm{in}} e^{\kappa t}$. Depending on the cooling rate κ, we find a crossover from effectively 1D behavior for rapid cooling to 2D behavior for slower cooling rates. Similar crossovers can also be observed for symmetry-breaking fields [70]. Exact analytic solution of the 1D case yields a scaling of the frozen correlation lengths $\xi_{\mathrm{freeze}} \propto \kappa^{-1/4}$. For the 2D case at intermediate cooling rates κ, we numerically found a scaling with $\kappa^{-\nu/(1+z\nu)} \approx \kappa^{-1/3}$, which is consistent with the Kibble–Zurek scaling in 2D. When comparing our results (e.g., that the cooling protocol can affect the anisotropy) with the experimental data in Fig. 1, we find that they match qualitatively but not quantitatively. Note that the exact cooling protocol for the sample in Fig. 1 is not precisely known. Whether the mismatch is caused by annealing after traversing the critical point (predominantly within the rows) or by the fact that parameters, such as the barrier height E_{B} and shape in Eq. (3), effectively deviate from the values we used should be investigated in future experiments by systematically varying the cooling rate. In this way, one can also turn the argument around: while the parameters in the Ising model (7) can be obtained from equilibrium measurements [52,53], these nonequilibrium scenarios facilitate experimental access to other parameters such as the knocking frequency Γ or the barrier height E_{B}. Our findings encourage further experimental investigations of the frozen domain structure for varying cooling rates in this anisotropic 2D Ising system in order to provide a well-controlled experimental approach to Kibble–Zurek dynamics in condensed matter.

Acknowledgments—Funded by the Deutsche Forschungsgemeinschaft (DFG, German Research Foundation) through the Collaborative Research Center SFB 1242 "Nonequilibrium dynamics of condensed matter in the time domain" (Project-ID 278162697).

[1] P. Bak and M. Paczuski, Complexity, contingency, and criticality, Proc. Natl. Acad. Sci. U.S.A. **92**, 6689 (1995).
[2] S. L. Sondhi, S. M. Girvin, J. P. Carini, and D. Shahar, Continuous quantum phase transitions, Rev. Mod. Phys. **69**, 315 (1997).
[3] S. Sachdev, *Quantum Phase Transitions* (Cambridge University Press, Cambridge, England, 2011).
[4] T. W. B. Kibble, Topology of cosmic domains and strings, J. Phys. A **9**, 1387 (1976).
[5] W. H. Zurek, Cosmological experiments in superfluid helium?, Nature (London) **317**, 505 (1985).
[6] T. W. B. Kibble and G. E. Volovik, On phase ordering behind the propagating front of a second-order transition, J. Exp. Theor. Phys. Lett. **65**, 102 (1997).
[7] W. H. Zurek, U. Dorner, and P. Zoller, Dynamics of a quantum phase transition, Phys. Rev. Lett. **95**, 105701 (2005).
[8] B. Damski, The simplest quantum model supporting the Kibble-Zurek mechanism of topological defect production: Landau-Zener transitions from a new perspective, Phys. Rev. Lett. **95**, 035701 (2005).
[9] L. Cincio, J. Dziarmaga, M. M. Rams, and W. H. Zurek, Entropy of entanglement and correlations induced by a quench: Dynamics of a quantum phase transition in the quantum Ising model, Phys. Rev. A **75**, 052321 (2007).
[10] A. Dutta, R. R. P. Singh, and U. Divakaran, Quenching through Dirac and semi-Dirac points in optical lattices:

Kibble-Zurek scaling for anisotropic quantum critical systems, Europhys. Lett. **89**, 67001 (2010).
[11] A. del Campo, G. De Chiara, G. Morigi, M. B. Plenio, and A. Retzker, Structural defects in ion chains by quenching the external potential: The inhomogeneous Kibble-Zurek mechanism, Phys. Rev. Lett. **105**, 075701 (2010).
[12] C.-W. Liu, A. Polkovnikov, and A. W. Sandvik, Dynamic scaling at classical phase transitions approached through nonequilibrium quenching, Phys. Rev. B **89**, 054307 (2014).
[13] P. M. Chesler, A. M. García-García, and H. Liu, Defect formation beyond Kibble-Zurek mechanism and holography, Phys. Rev. X **5**, 021015 (2015).
[14] J. Sonner, A. del Campo, and W. H. Zurek, Universal far-from-equilibrium dynamics of a holographic superconductor, Nat. Commun. **6**, 7406 (2015).
[15] P. Silvi, G. Morigi, T. Calarco, and S. Montangero, Crossover from classical to quantum Kibble-Zurek scaling, Phys. Rev. Lett. **116**, 225701 (2016).
[16] D. Jaschke, K. Maeda, J. D. Whalen, M. L. Wall, and L. D. Carr, Critical phenomena and Kibble–Zurek scaling in the long-range quantum Ising chain, New J. Phys. **19**, 033032 (2017).
[17] B. Dóra, M. Heyl, and R. Moessner, The Kibble-Zurek mechanism at exceptional points, Nat. Commun. **10**, 2254 (2019).
[18] R. Puebla, O. Marty, and M. B. Plenio, Quantum Kibble-Zurek physics in long-range transverse-field Ising models, Phys. Rev. A **100**, 032115 (2019).
[19] L. Ulčakar, J. Mravlje, and T. Rejec, Kibble-Zurek behavior in disordered Chern insulators, Phys. Rev. Lett. **125**, 216601 (2020).
[20] K. Hódsági and M. Kormos, Kibble–Zurek mechanism in the Ising field theory, SciPost Phys. **9**, 055 (2020).
[21] H. Oshiyama, N. Shibata, and S. Suzuki, Kibble–Zurek mechanism in a dissipative transverse Ising chain, J. Phys. Soc. Jpn. **89**, 104002 (2020).
[22] C. J. O. Reichhardt, A. del Campo, and C. Reichhardt, Kibble-Zurek mechanism for nonequilibrium phase transitions in driven systems with quenched disorder, Commun. Phys. **5**, 173 (2022).
[23] Á. Bácsi and B. Dóra, Kibble–Zurek scaling due to environment temperature quench in the transverse field Ising model, Sci. Rep. **13**, 4034 (2023).
[24] A. Weitzel, G. Schaller, F. Queisser, and R. Schützhold, Continuous dimer angles on the silicon surface: Critical properties and the Kibble-Zurek mechanism, Phys. Rev. B **110**, 245125 (2024).
[25] V. M. H. Ruutu, V. B. Eltsov, A. J. Gill, T. W. B. Kibble, M. Krusius, Yu G. Makhlin, B. Plaçais, G. E. Volovik, and Wen Xu, Vortex formation in neutron-irradiated superfluid ^{3}He as an analogue of cosmological defect formation, Nature (London) **382**, 334 (1996).
[26] V. B. Eltsov, T. W. B. Kibble, M. Krusius, V. M. H. Ruutu, and G. E. Volovik, Composite defect extends analogy between cosmology and ^{3}He, Phys. Rev. Lett. **85**, 4739 (2000).
[27] S. Ulm, J. Roßnagel, G. Jacob, C. Degünther, S. T. Dawkins, U. G. Poschinger, R. Nigmatullin, A. Retzker, M. B. Plenio, F. Schmidt-Kaler, and K. Singer, Observation of the Kibble-Zurek scaling law for defect formation in ion crystals, Nat. Commun. **4**, 2290 (2013).
[28] G. Lamporesi, S. Donadello, S. Serafini, F. Dalfovo, and G. Ferrari, Spontaneous creation of Kibble–Zurek solitons in a Bose–Einstein condensate, Nat. Phys. **9**, 656 (2013).
[29] S. Deutschländer, P. Dillmann, G. Maret, and P. Keim, Kibble–Zurek mechanism in colloidal monolayers, Proc. Natl. Acad. Sci. U.S.A. **112**, 6925 (2015).
[30] M. Gong, X. Wen, G. Sun, D.-W. Zhang, D. Lan, Y. Zhou, Y. Fan, Y. Liu, X. Tan, H. Yu, Y. Yu, S.-L. Zhu, S. Han, and P. Wu, Simulating the Kibble-Zurek mechanism of the Ising model with a superconducting qubit system, Sci. Rep. **6**, 22667 (2016).
[31] J. Beugnon and N. Navon, Exploring the Kibble–Zurek mechanism with homogeneous Bose gases, J. Phys. B **50**, 022002 (2017).
[32] L.-Y. Qiu, H.-Y. Liang, Y.-B. Yang, H.-X. Yang, T. Tian, Y. Xu, and L.-M. Duan, Observation of generalized Kibble-Zurek mechanism across a first-order quantum phase transition in a spinor condensate, Sci. Adv. **6**, eaba7292 (2020).
[33] J. Rysti, J. T. Mäkinen, S. Autti, T. Kamppinen, G. E. Volovik, and V. B. Eltsov, Suppressing the Kibble-Zurek mechanism by a symmetry-violating bias, Phys. Rev. Lett. **127**, 115702 (2021).
[34] K. Du, X. Fang, C. Won, C. De, F.-T. Huang, W. Xu, H. You, F. J. Gómez-Ruiz, A. del Campo, and S.-W. Cheong, Kibble–Zurek mechanism of Ising domains, Nat. Phys. **19**, 1495 (2023).
[35] B.-W. Li, Y.-K. Wu, Q.-X. Mei, R. Yao, W.-Q. Lian, M.-L. Cai, Y. Wang, B.-X. Qi, L. Yao, L. He, Z.-C. Zhou, and L.-M. Duan, Probing critical behavior of long-range transverse-field Ising model through quantum Kibble-Zurek mechanism, PRX Quantum **4**, 010302 (2023).
[36] T. D. Schultz, D. C. Mattis, and E. H. Lieb, Two-dimensional Ising model as a soluble problem of many fermions, Rev. Mod. Phys. **36**, 856 (1964).
[37] B. M. McCoy and T. T. Wu, *The Two-Dimensional Ising Model* (Harvard University Press, Harvard, 1973).
[38] R. J. Baxter, *Exactly Solved Models in Statistical Mechanics* (Academic Press, London, 1989).
[39] M. A. Neto, R. A. dos Anjos, and J. R. de Sousa, Anisotropic Ising model in a magnetic field: Effective-field theory analysis, Phys. Rev. B **73**, 214439 (2006).
[40] H. Hobrecht and A. Hucht, Anisotropic scaling of the two-dimensional Ising model I: The torus, SciPost Phys. **7**, 26 (2019).
[41] H. Hobrecht and A. Hucht, Anisotropic scaling of the two-dimensional Ising model II: surfaces and boundary fields, SciPost Phys. **8**, 32 (2020).
[42] A. Hucht, The square lattice Ising model on the rectangle III: Hankel and Toeplitz determinants, J. Phys. A **54**, 375201 (2021).
[43] H. J. W. Zandvliet, Phase diagram of the square 2D Ising lattice with nearest neighbor and next-nearest neighbor interactions, Phase Transitions **96**, 187 (2023).
[44] A. Saxena, E. T. Gawlinski, and J. D. Gunton, Structural phase transitions on the Si(100) surface, Surf. Sci. **160**, 618 (1985).

[45] M. Kubota and Y. Murata, Streak patterns in low-energy electron diffraction on Si(001), Phys. Rev. B **49**, 4810 (1994).
[46] Y. Murata and M. Kubota, Order-disorder transition on Si(001), Phase Transitions **53**, 125 (1995).
[47] K. Inoue, Y. Morikawa, K. Terakura, and M. Nakayama, Order-disorder phase transition on the Si(001) surface: Critical role of dimer defects, Phys. Rev. B **49**, 14774(R) (1994).
[48] Y. Nakamura, H. Kawai, and M. Nakayama, Influence of defects on the order-disorder phase transition of a Si(001) surface, Phys. Rev. B **55**, 10549 (1997).
[49] H. Kawai, Y. Nakamura, and M. Nakayama, Kinetic one-dimensional Ising system on a narrow $\mathrm{Si}(001)\mathrm{S_B}$ terrace, J. Phys. Soc. Jpn. **68**, 3936 (1999).
[50] D. Pillay, B. Stewart, C. B. Shin, and G. S. Hwang, Revisit to the Ising model for order–disorder phase transition on Si(001), Surf. Sci. **554**, 150 (2004).
[51] H. Kawai, O. Narikiyo, and K. Matsufuji, Structural phase transition between $c(4\times 2)$ and $p(2\times 2)$ structures on Si(001) surface under observation by scanning tunneling microscopy, J. Phys. Soc. Jpn. **76**, 034602 (2007).
[52] C. Brand, A. Hucht, G. Jnawali, J. D. Fortmann, B. Sothmann, H. Mehdipour, P. Kratzer, R. Schützhold, and M. Horn-von Hoegen, Dimer coupling energies of the Si(001) surface, Phys. Rev. Lett. **130**, 126203 (2023).
[53] C. Brand, A. Hucht, H. Mehdipour, G. Jnawali, J. D. Fortmann, M. Tajik, R. Hild, B. Sothmann, P. Kratzer, R. Schützhold, and M. Horn-von Hoegen, Critical behavior of the dimerized Si(001) surface: Continuous order-disorder phase transition in the two-dimensional Ising universality class, Phys. Rev. B **109**, 134104 (2024).
[54] R. A. Wolkow, Direct observation of an increase in buckled dimers on Si(001) at low temperature, Phys. Rev. Lett. **68**, 2636 (1992).
[55] R. G. Zhao and W. S. Yang, Atomic structure of the Si(001) $\mathrm{c}(4\times 2)$ surface, Phys. Rev. B **33**, 6780 (1986).
[56] Y. Pennec, M. Horn-von Hoegen, Xiaobin Zhu, D. C. Fortin, and M. R. Freeman, Dynamics of an Ising chain under local excitation: A scanning tunneling microscopy study of Si(100) dimer rows at 5 K, Phys. Rev. Lett. **96**, 026102 (2006).
[57] D. S. Fisher, Scaling and critical slowing down in random-field Ising systems, Phys. Rev. Lett. **56**, 416 (1986).
[58] J. R. Tredicce, G. L. Lippi, Paul Mandel, B. Charasse, A. Chevalier, and B. Picqué, Critical slowing down at a bifurcation, Am. J. Phys. **72**, 799 (2004).
[59] See Supplemental Material at http://link.aps.org/supplemental/10.1103/rmc4-xqb3 for a brief review of the Kibble-Zurek argument, the derivation and solution of the time-dependent 1D Ising model equations, the derivation and approximate solution of the time-dependent 2D Ising model equations, and an exposure of the numerical methods.
[60] J. Dąbrowski, E. Pehlke, and M. Scheffler, Calculation of the surface stress anisotropy for the buckled $\mathrm{Si}(001)(1\times 2)$ and $\mathrm{p}(2\times 2)$ surfaces, Phys. Rev. B **49**, 4790 (1994).
[61] R. J. Glauber, Time-dependent statistics of the Ising model, J. Math. Phys. (N.Y.) **4**, 294 (1963).
[62] Y. Sakai and K. Hukushima, Dynamics of one-dimensional Ising model without detailed balance condition, J. Phys. Soc. Jpn. **82**, 064003 (2013).
[63] A. O. Caldeira, A. H. Castro Neto, and T. Oliveira de Carvalho, Dissipative quantum systems modeled by a two-level-reservoir coupling, Phys. Rev. B **48**, 13974 (1993).
[64] C. Timm, Tunneling through molecules and quantum dots: Master-equation approaches, Phys. Rev. B **77**, 195416 (2008).
[65] L. Onsager, Crystal statistics. I. A Two-dimensional model with an order-disorder transition, Phys. Rev. **65**, 117 (1944).
[66] F. M. Bulnes, V. D. Pereyra, and J. L. Riccardo, Collective surface diffusion: *n*-fold way kinetic Monte Carlo simulation, Phys. Rev. E **58**, 86 (1998).
[67] K. Binder and D. W. Heermann, *Rejection-Free Monte Carlo* (Springer International Publishing, Cham, 2019), pp. 179–190.
[68] P. Kratzer, Monte Carlo and Kinetic Monte Carlo methods—A tutorial, in *Multiscale Simulation Methods in Molecular Sciences*, Volume 42 of NIC Series (John von Neumann Institute for Computing (NIC), Jülich Supercomputing Centre, Forschungszentrum Jülich, Jülich, Germany, 2009), pp. 51–76.
[69] R. M. Tromp and M. C. Reuter, Step morphologies on small-miscut Si(001) surfaces, Phys. Rev. B **47**, 7598 (1993).
[70] F. Suzuki and W. H. Zurek, Topological defect formation in a phase transition with tunable order, Phys. Rev. Lett. **132**, 241601 (2024).